Redox Cycling in Nanoscale-Recessed Ring-Disk Electrode Arrays for Enhanced Electrochemical Sensitivity

Chaoxiong Ma,[†] Nicholas M. Contento,[‡] Larry R. Gibson II,[‡] and Paul W. Bohn[†,‡,*]

[†]Department of Chemistry and Biochemistry and [‡]Department of Chemical and Biomolecular Engineering, University of Notre Dame, Notre Dame, Indiana 46556, United States

ABSTRACT An array of nanoscale-recessed ring-disk electrodes was fabricated using layer-by-layer deposition, nanosphere lithography, and a multistep reactive ion etching process. The resulting device was operated in generator–collector mode by holding the ring electrodes at a constant potential and performing cyclic voltammetry by sweeping the disk potential in $Fe(CN)_6^{3-/4-}$ solutions. Steady-state response and enhanced (~10×) limiting current were achieved by cycling the redox couple between ring and disk electrodes with high transfer/collection efficiency. The collector (ring) electrode, which is held at a constant potential, exhibits a much smaller charging current than the generator (disk), and it is relatively insensitive to scan rate. A characteristic feature of the nanoscale ring–disk geometry is that the electrochemical reaction occurring at the disk electrodes can be tuned by modulating the potential at the ring electrodes. Measured shifts in $Fe(CN)_6^{3-/4-}$ concentration profiles were found to be in excellent agreement with finite element method simulations. The main performance metric, the amplification factor, was optimized for arrays containing small diameter pores ($r < 250$ nm) with minimum electrode spacing and high pore density. Finally, integration of the fabricated array within a nanochannel produced up to 50-fold current amplification as well as enhanced selectivity, demonstrating the compatibility of the device with lab-on-a-chip architectures.

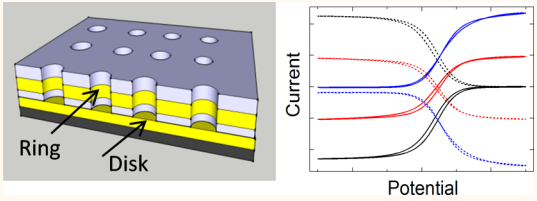

KEYWORDS: redox cycling · nanoelectrode array · recessed ring-disk electrode · generator–collector · nanofluidic · current amplification

In the last two decades, micro/nanoelectrode systems have been extensively studied for electrochemical analysis[1−6] and biosensing[7−10] because of several well-established advantages, such as fast response times, small capacitive currents, and enhanced steady-state voltammetric response compared to macroelectrode systems.[11] To extend the benefits of ultramicroelectrode behavior, electrode ensembles or arrays[2,5,12−15] are commonly used to enhance faradaic currents, while retaining most of the other benefits of using a single micro/nanoelectrode. An interesting example is the interdigitated electrode array (IDA),[12,13,16−20] where two electrodes are configured as closely spaced parallel bands, such that concentration profiles of redox species overlap, allowing the species generated at one electrode to be efficiently collected at a neighboring electrode. The resulting redox cycling (RC) effect, although most widely studied in IDAs,[12,13,16,19−22] can also be observed in other geometries with closely spaced electrodes, such as triple band electrodes,[23,24] thin layer cells,[10,25,26] and the recently developed ring/plane-recessed disk electrodes.[8,27−32]

The RC effect, arising from the operation of these devices in generator–collector (GC) mode,[13,22] is crucial as both a test of theory and for practical applications. In addition to enhanced faradaic currents, selectivity is also improved in devices using the RC effect because in a well-designed experiment only the current from the targeted reversible redox analyte is amplified.[10,19,31] Furthermore, small charging currents can be achieved at collector electrodes held at a constant potential,[13] allowing for fast scan cyclic voltammetry (CV) measurements. GC geometries have been used to determine the diffusion coefficients of redox species based on electrochemical time-of-flight response[33,34] and to investigate electrochemical reaction mechanisms by monitoring the lifetime of electrogenerated intermediates.[21,22,30,32] Similar strategies using the RC effect have

* Address correspondence to pbohn@nd.edu.

Received for review March 28, 2013 and accepted May 21, 2013.

Published online May 21, 2013
10.1021/nn401542x

also been employed for selective detection of target analytes based on differences in redox reversibility.[10,19,25,31] Reversibility is obviously a key requirement in these experiments, with irreversible redox processes not being observable because the initial redox species is not regenerated at the collector electrode.[10,35] Alternatively, by setting the generator electrode at an appropriate potential, irreversible redox species can be depleted before diffusing to the collector.[31] In both instances, reversible target molecules can be detected from the collector electrode signal without interference from irreversible species in the sample.

Importantly, improved performance can be achieved by decreasing the interelectrode distance of the devices[10,25,27,31,32] because smaller electrode spacing produces higher collection efficiency and current amplification, leading to higher sensitivity and selectivity. In addition, devices with reduced size are compatible with lab-on-a-chip devices characterized by small sample volumes, a critical criterion for measurements of mass-limited samples. While photolithography can produce electrodes with micrometer-scale spacing, fabrication of devices with nanometer-scale features usually requires electron-beam lithography,[5,13,14,19,36] which is costly, low-throughput, and time-consuming.

In this study, arrays of recessed ring-disk electrodes with nanoscale interelectrode distances are fabricated using layer-by-layer deposition followed by nanosphere lithography[5,37] (NSL) and a multistep etching process. Similar approaches have been used to fabricate micrometer-scale devices[3,8,27,38−40] with recessed band-disk electrodes inside a single cavity, characterized and applied to biosensing by Fritsch and co-workers. In addition, Compton *et al.* fabricated, characterized, and theoretically studied micrometer-scale arrays of ring-recessed disk electrodes.[22,29,30,32] The plane-recessed disk array electrodes[28,31] have also been constructed and applied to the detection of pyrocatechol and dopamine in the presence of interferences. These studies demonstrate some promising advantages of the ring-disk geometry and suggest that shrinking electrode size and interelectrode spacing to the nanoscale could further enhance device performance.

Here, we report a robust procedure for the fabrication of an array of recessed ring-disk electrodes with both electrode size and spacing at the nanometer scale. Arrays with varying insulator thickness and pore density were fabricated and characterized by cyclic voltammetry employing the disks and rings as generator and collector electrodes, which are swept and held at a constant potential, respectively. The effect of design parameters on the collection efficiency, current amplification, and conversion ratio are all reported here. To understand the influence of collector potential on reactions at the generator, finite element method simulations are performed and compared with experimental results. In order to evaluate performance in a confined geometry and explore its utility for lab-on-a-chip applications, the device was studied in both open and nanochannel-confined geometries. The nanochannel-confined geometry produces higher collection efficiency, current amplification, and selectivity for GC operation compared to the open geometry.

RESULTS AND DISCUSSION

Current Amplification in Generator−Collector Mode. In the fabrication approach used here, electrodes are embedded in zero-dimensional nanopores, where interelectrode distance is controlled by the thickness of the insulator separating the two electrodes (viz. Figure 1). Thin (∼100 nm) films of SiN_x deposited by plasma-enhanced chemical vapor deposition provide excellent electrical isolation of the two working electrodes. NSL is used for patterning because of its simplicity and its capability to produce ordered arrays of electrodes with controllable size and spacing.[5,37] Pore size is controlled by the diameter of the polystyrene spheres used to template NSL, and pores are etched through to the underlying Au layer by a multistep reactive ion etching (RIE) process, thus producing an array of nanometer-scale recessed ring-disk electrodes.

SEM images of the nanofabricated electrode array are shown in Figure 1, from which an average radius (r) of the nanopores containing the ring/disk electrodes is determined to be 234 ± 12 nm with an interelectrode spacing of ∼1.0 μm (d). In this electrode geometry ($d \approx 4r$), diffusion zones of the individual disk electrodes exhibit substantial overlap (see Figure S2, Supporting Information), and the electrode array is expected to behave like a planar electrode with an area equal to that of the entire array,[41] that is, 50 μm × 50 μm.

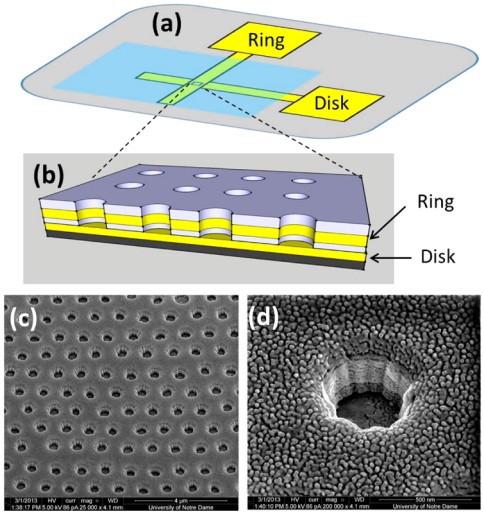

Figure 1. (a) Schematic diagram showing the macroscopic layout of the device and (b) ring-disk geometry in the nanopores. (c) SEM image of the array at 52° tilt; (d) magnified view for a single electrode at 52° tilt.

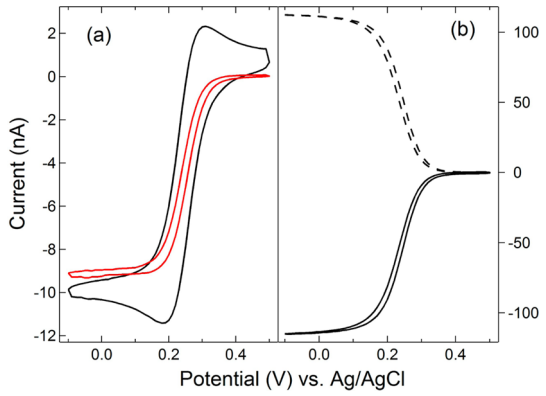

Figure 2. Comparison of GC and non-GC mode cyclic voltammograms of 1 mM $Fe(CN)_6^{3-}$ solution on a high density array with a 200 nm insulator separating the ring and disk electrodes. (a) Non-GC mode: ring electrodes are floating, and disk electrodes are swept at 100 mV/s (black) and 5 mV/s (red). (b) GC mode: disk (solid) and ring (dashed) current for ring electrodes held 0.5 V and disk electrodes swept at 100 mV/s.

This predicted behavior can be compared against the cyclic voltammograms (CVs) of the disk electrode array shown in Figure 2a, which were measured in 1.0 mM $K_3Fe(CN)_6$ and 2.0 M KCl with the ring electrodes floating. As seen in Figure 2a, CV measurements at 100 mV/s produce a transient response with a slow decay of the faradaic current plateau. At a scan rate of 5 mV/s, a pseudo-steady-state response with limiting current of 9.3 nA was observed. This behavior is in good agreement with that of a recessed microelectrode with size of 50 μm × 50 μm and a recessed depth of 0.6 μm (see Figure S3, Supporting Information). A limiting current of ~8.1 nA is estimated from the expression for current at a recessed microelectrode[42,43]

$$I_{lim} = \frac{4\pi nFDCr_a^2}{4H + \pi r_a} \quad (1)$$

where n is the number of electrons transferred, D is the diffusion coefficient, C is the bulk concentration, H is the recessed depth, and r_a (28 μm) is the apparent radius of the microelectrode. The small discrepancy between the observed current and that calculated from eq 1 is likely the result of edge effects, which enhance the signal from electrodes at the periphery of the array, resulting in an increase in actual electrode area relative to the estimated geometric area.

Figure 2b shows the CV responses of the electrode array at 100 mV/s in GC mode, where the potential of the ring (collector) electrodes is maintained at 0.5 V. Quantitatively reproducible voltammetry is observed at both generator and collector electrodes with a limiting current of 95 nA, which is ~10 times larger than the current collected at the disk electrode with the ring electrodes floating (non-GC mode). This strong current amplification is attributed to redox cycling of the electroactive species between generator and collector electrodes. The RC effect depends strongly on the collection efficiency, Φ, with which the collector electrodes collect species generated at the generator.[13] Under the conditions of Figure 2b, the collection efficiency of the ring electrodes, Φ_r, is

$$\Phi_r = \frac{i_{r,a}}{i_{d,c}} \quad (2)$$

where $i_{r,a}$ and $i_{d,c}$ are the anodic and cathodic limiting currents at the ring and disk electrodes, respectively. Using eq 2, Φ_r = 0.98 was obtained from the results shown in Figure 2b.

Effect of Ring Electrode Potential. In the preceding experiments, the collector (ring) electrodes are held at an anodic potential, E = 0.5 V *vs* Ag/AgCl, in order to oxidize the $Fe(CN)_6^{4-}$, generated at the disk electrodes, back to $Fe(CN)_6^{3-}$, which then diffuses back to the disk electrodes for re-reduction. This diffusion-controlled electrochemical loop enables the RC behavior, which is the principal goal of constructing these nanoscale-recessed ring-disk arrays. Although it is most common to effect GC mode measurements with the collector regenerating the initial species (in this case, $Fe(CN)_6^{3-}$), modulation of the ring electrodes to more cathodic potentials can also be useful in order to differentiate two or more different electroactive species,[25,31,44] to mitigate interferences,[10,19,31] or to determine fast electron-transfer kinetics.[45] Accordingly, the effect of the ring electrode potential on the CV response of the disk electrodes was investigated both experimentally and theoretically.

Experimental CV scans on the fabricated array and finite element simulations on an array of 10 recessed ring-disk electrodes, shown in Figure 3a,b, are in good agreement, both in shape and potential dependence. When the fixed potential of the ring electrodes is 0.5 V (black curve in Figure 3a), the anodic current is collected at the rings and the cathodic current is collected at the disks in the cathodic region of the disk potential, *ca.* −0.1 to 0.25 V *vs* Ag/AgCl. As shown in Figure 3b, similar behavior is observed in the simulation for an array of 10 recessed ring-disk electrodes. The disk current of a single electrode (~0.074 nA) derived from Figure 3b can be scaled up by a factor of ~1530 to be in line with experimentally observed current from the entire array. This scaling factor is close to the number of pores, ~2000, with the remaining discrepancy likely resulting from edge effects, which are accentuated in the simulation.

Conversely, when the fixed potential of the ring electrodes is set at the relatively cathodic value of −0.1 V *vs* Ag/AgCl (blue curves in Figure 3a,b), cathodic current is collected at the rings and anodic current is collected at the disks in the anodic region of the disk potential, *ca.* 0.25 to 0.5 V *vs* Ag/AgCl. Finally, poising the ring electrodes at the intermediate potential of 0.25 V *vs* Ag/AgCl (red curves in Figure 3a,b) yields intermediate behavior with anodic (cathodic) current

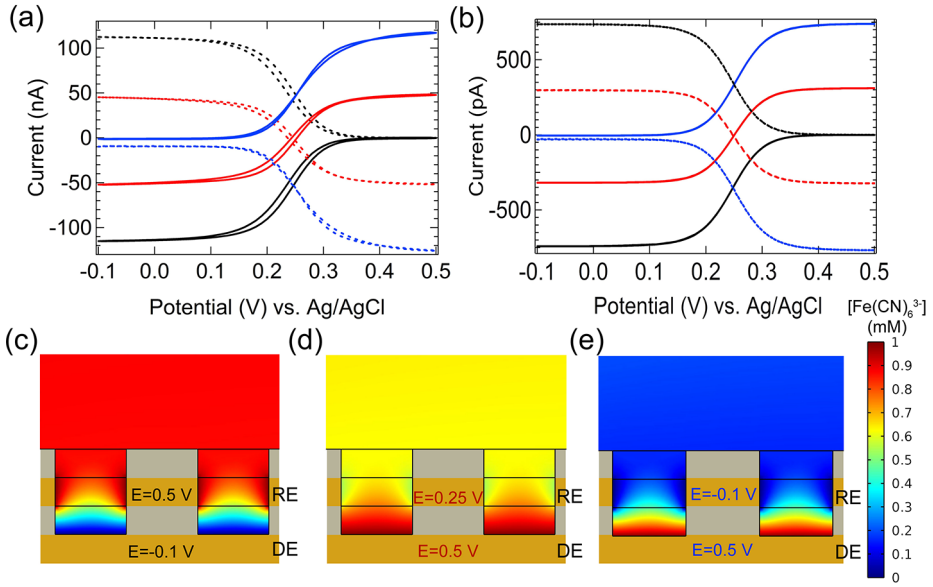

Figure 3. (a) Ring potential dependence of voltammetric response of 1 mM $Fe(CN)_6^{3-}$ solution on a high density array with 200 nm insulator. Disk electrodes are swept at 100 mV/s, and ring electrodes are held at 0.5 V (black), 0.25 V (red), and −0.1 V (blue); disk current (solid) and ring current (dashed). (b) Finite element simulated CV response of an array of 10 electrodes in 1 mM $Fe(CN)_6^{3-}$ solution on a high density array with 200 nm insulator with the ring electrode held at 0.5 V (black), 0.25 V (red), and −0.1 V (blue). (c−e) Concentration profiles of $Fe(CN)_6^{3-}$ in adjacent pores with a radius of 250 nm taken from simulations of an array of 10 electrodes. The height of the insulator layers (gray) and the ring electrode (yellow) is 200 nm.

collected at the rings (disks) with the disk potential in the range of −0.1 to 0.2 V and cathodic (anodic) current collected at the rings (disks) with the disk potential in the range of 0.3 to 0.5 V. A crossover region is observed when the disk potential is in the range of 0.2 to 0.3 V. The current is much larger for a collection of single nanoelectrodes, which operate under radial diffusion, than for the high density electrode array, in which overlapping diffusion zones produce behavior approaching that of a planar electrode. An increase in relative cathodic current offset is also seen in experiments with low density nanopore arrays (data not shown), supporting the interpretation that diffusion zone overlap is the main reason the current offset decreases.

In agreement with previous results,[45] only cathodic current is observed at the disk electrodes when ring electrodes are held at the oxidative potential of 0.5 V. This is further confirmed by the calculated concentration profile of $Fe(CN)_6^{3-}$ in the nanopore shown in Figure 3c. Only oxidized species are available to the disks because the rings rapidly oxidize all $Fe(CN)_6^{4-}$ generated at the disks. When the ring electrodes are held at 0.25 V, near E_{eq}, both anodic and cathodic currents are observed at the disks. The concentration profile of $Fe(CN)_6^{3-}$ for $E_{ring} = 0.25$ V and $E_{disk} = 0.5$ V is shown in Figure 3d. The rings do not consume all the $Fe(CN)_6^{4-}$ produced, leaving both species available for oxidation and reduction at the disks. When the ring electrodes are held at −0.1 V, current at the disks is mostly anodic since $Fe(CN)_6^{3-}$ is depleted at the rings, as seen in Figure 3e. Experimentally, a constant offset of ∼9 nA is observed for the cathodic current at the rings, which is approximately 5−10 times higher than the current of the disks at −0.1 V, a difference that could result from the asymmetry of the electrode geometry; that is, the $Fe(CN)_6^{3-}$ can more easily access the rings than the disks even when both electrodes are held at −0.1 V. Also, this offset current is similar in magnitude to that observed for disk electrodes in the non-GC configuration (cf. Figure 2a). The constant current offset is the steady-state current achieved by poising the ring electrodes at a constant reducing potential, causing the array to act as a single planar electrode.

For the same geometrical reason, the collection efficiency of the disks Φ_d is expected to be smaller than that of the rings, Φ_r. Φ_d can be estimated by holding the disks at 0.5 V while sweeping the potential of the rings or by using the limiting disk and ring currents in Figure 3 when the rings are held at −0.1 V. In both cases, $Fe(CN)_6^{4-}$ generated at the rings is collected by and oxidized at the disks, with Φ_d then being determined by

$$\Phi_d = \frac{i_{d,a}}{i_{r,c}} \quad (3)$$

where $i_{d,a}$ and $i_{r,c}$ are the anodic and cathodic limiting currents at the disk and ring electrodes, respectively. $\Phi_d = 0.92$ was obtained from the results (blue curves) in Figure 3a. Using the method proposed by Tabei *et al.*,[13] the number of redox cycling events, N_{rc}, is directly related to the current amplification and is given by

$$N_{rc} = \frac{1}{1 - \Phi_r\Phi_d} \quad (4)$$

TABLE 1. Effect of Array Parameters on Device Performance

electrode separation (nm)	Φ_r	Φ_d	AF[a]	N_{rc}	η
100	0.98	0.91	12.3	12.5	0.98
200	0.98	0.90	7.8	8.3	0.99
300	0.96	0.84	5.2	5.5	0.97
300 (low density[b])	0.74	0.34	1.4	1.4	0.67

[a] Amplification factor, defined by the ratio of the cathodic current in GC and non-GC modes. [b] Low density refers to an electrode array containing ~15 electrodes occupying the same area as a high density array containing ~2000 electrodes.

For the device described, Φ_r = 0.98 and Φ_d = 0.92, yielding N_{rc} = 10.2, consistent with current amplification of 11.5, calculated directly from the limiting currents of the cyclic voltammograms.

For IDAs, the influence of one electrode on the response of its neighbors is quantified through a shielding factor.[12,46] In this study, this effect is estimated more directly by the ratio of the electroactive species from bulk solution being converted (oxidized or reduced) to its conjugated redox form before reacting at the disks. For $Fe(CN)_6^{3-}$, the conversion ratio, η, which quantifies the reduction of $Fe(CN)_6^{3-}$ to $Fe(CN)_6^{4-}$ at the ring electrodes, is given by

$$\eta = \frac{i_{d,a}}{i_{d,tot}} \quad (5)$$

where $i_{d,a}$ is the anodic current and $i_{d,tot} = |i_{d,c}| + |i_{d,a}|$ is the sum of the cathodic and anodic current at the disk electrodes when the ring electrodes are held at −0.1 V. A high conversion ratio is useful for selective detection or the depletion of interfering species. A value of 0.99 was obtained from the CV results (solid blue curve) in Figure 3a, which could improve selectivity 100-fold when using the rings to deplete an irreversible redox interference.

Effect of Insulator Thickness and Electrode Density. The electrode separation, that is, the distance between the disk and ring electrodes, which is governed by the insulator thickness, is a major determinant of device performance, as summarized in Table 1. Collection efficiency decreases at both ring and disk electrodes with increasing insulator thickness, with the dependence of Φ_d being stronger than that of Φ_r. This observation is likely due to species generated at the rings taking longer to diffuse to the disks as the electrode separation is increased, thus increasing the probability that the species will diffuse into bulk solution and be lost to RC. This effect is less significant for species generated at the disks because species generated at the disks must diffuse past the rings to get to bulk solution.

N_{rc} depends strongly on both collection efficiencies, and since both decrease with increasing electrode separation distance, N_{rc} also decreases. This dependence on electrode separation is consistent with the current amplification factor, AF, which agrees well with the calculated values of N_{rc}.

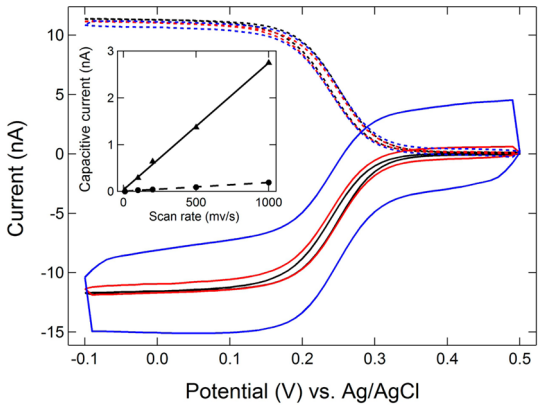

Figure 4. Scan rate dependence of voltammograms of 0.1 mM $Fe(CN)_6^{3-}$ solution on a high density array with 200 nm insulator. Disk electrodes are swept at 10 mV/s (black), 100 mV/s (red), and 1000 mV/s (blue), and ring electrodes are held at 0.5 V; disk current (solid) and ring current (dashed). (Inset) Capacitive current as a function of scan rate for disk (solid) and ring (dashed) electrodes.

It is interesting to note that the conversion ratio is less sensitive to changes in electrode separation distance. This is likely due to the fact that both reduced and oxidized forms of the redox couple share the same diffusional path and are affected by the electrode separation distance in the same way. Hence, changes in electrode separation do not significantly affect the ratio of the two redox forms reaching the disk electrodes.

As discussed above, an array of recessed ring-disk electrodes exhibits a distinct CV response compared to a single recessed ring-disk electrode. The effect of electrode density on the properties of the device was investigated by conducting the same measurements on devices with ~15 pores in a 50 μm × 50 μm area (viz. Table 1). It can be seen that collection efficiency, amplification factor, and conversion ratio are all reduced for isolated electrodes, relative to arrays with overlapping diffusion zones. Arrays are characterized by higher collection efficiency because species generated in one nanopore could be collected by electrodes in an adjacent nanopore. For the same reason, larger conversion ratios can be obtained in high density electrode arrays since neighboring ring electrodes can facilitate the depletion (conversion) of the species from the bulk solution before they reach the disks. The influence of the electrode density on the array performance is also consistent with simulation results (Table S1, Supporting Information). While low density arrays are used in applications where it is desirable to avoid overlapping diffusion zones, this is not necessary for the nanoscale-recessed ring-disk array used in GC mode, which exhibits steady-state waves at both generator and collector, regardless of electrode density at all experimental time scales studied here.

Scan Rate Dependence. The scan rate dependence of CV measurements of devices operated in GC mode is shown in Figure 4. Steady-state voltammetric response

is obtained at both the generator and the collector electrodes at all scan rates between 10 and 1000 mV/s. A useful characteristic property of GC mode operation is the small charging current at the constant potential collector (rings).[13,16] On the other hand, charging current at the generator (disks) is obviously much more susceptible to changing scan rate (inset of Figure 4). It should be noted that a small, scan-rate-dependent charging current (dashed line, Figure 4 inset) is observed at the ring electrodes, even though they are held at constant potential. This observation is attributed to imperfect insulation between the ring and disk electrodes which leads to charge leakage and the small charging current observed on the ring electrodes. The charging current at the collector is ~10-fold smaller than that at the generator at 1000 mV/s, demonstrating that the collector signal is better poised for high scan rate operation.

Integration of the Array in a Nanochannel. One important goal of this study is to study the applicability of the fabricated device to lab-on-a-chip systems, in which integrated micro- or nanofluidic channels allow for intelligent control over analyte delivery. Amperometric measurements within a confined geometry such as micro- or nanochannels can be challenging[19,39,46] because the diffusive boundary layer arising from the small channel height can depress the faradaic signal, leading to diminished steady-state voltammetric response. To investigate the application of the nanoscale array for measurements inside a confined geometry, a channel of 200 nm depth, 25 μm width, and ~5 mm length was integrated with the nanoelectrode array, and the resulting 25 μm × 50 μm recessed ring-disk electrode array was characterized by cyclic voltammetry.

Figure 5 shows CV measurements conducted in both GC and non-GC modes in the nanofluidic channel. In non-GC mode, a transient, peak-shaped curve with both oxidation and reduction currents is observed, which, after normalizing for differences in array size, yields a much smaller current magnitude than that for the open array shown in Figure 2a. The lower current is attributed to depletion of $Fe(CN)_6^{3-}$ from the channel due to the limited rate of diffusion to the channel opening. The confined geometry of the channel also slows the diffusion of $Fe(CN)_6^{4-}$ generated on the disk electrodes away from the array, leading to an oxidative peak, which is not observed in the open channel geometry.

In GC mode, Figure 5b, steady-state waves are observed, which are similar to those obtained in the open geometry (cf. Figure 2b). In addition, there is no obvious decrease in the limiting current if the size of the array is taken into account, indicating that the redox cycling effect and the performance of the array are not significantly affected by the channel geometry. Interestingly, higher values (~0.99) of collection efficiencies and conversion ratio are also obtained for

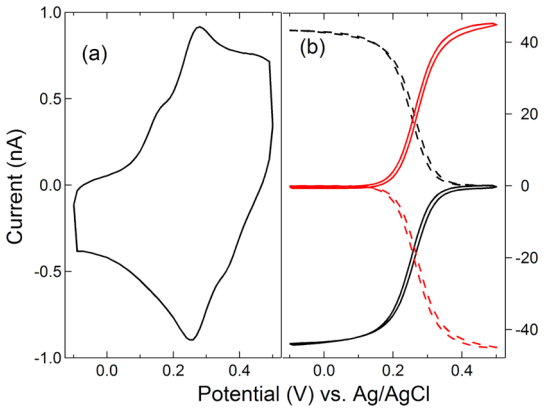

Figure 5. Cyclic voltammograms using an array integrated with a nanochannel. The CVs were measured in 1 mM $Fe(CN)_6^{3-}$ solution on a high density array with a 200 nm insulator. Disk electrodes are swept at 100 mV/s. (a) Ring electrodes disconnected (non-GC mode); (b) ring electrodes held at 0.5 V (black) or −0.1 V (red). Disk current (solid) and ring current (dashed).

measurements in the nanochannel. For example, $N_{rc} \sim 50$ is obtained in the nanochannel configuration, in agreement with current amplification factor, AF ~ 63, derived from the limiting (44 nA) and peak currents (0.7 nA) in Figure 5. A higher conversion ratio is useful when the rings are used for depletion of interference or selective detection of two species with different redox potential. Thus, these results demonstrate that nanoscale-recessed ring-disk arrays can be used for amperometric measurements in microchannel- and nanochannel-confined geometries without diminishing the steady-state response. Therefore, integrating these devices within nanochannels should provide access to amperometric measurements with improved sensitivity and selectivity.

CONCLUSIONS

A simple, massively parallel scheme employing NSL for producing complex arrays of coupled nanoscale working electrodes is described. The arrays of recessed ring-disk electrodes fabricated in this way display nanoscale interelectrode spacings which allow redox cycling of the electroactive species between ring and disk electrodes, producing amplified steady-state currents. When operated in the generator−collector mode, dramatic improvements in electrochemical performance can be realized relative to non-GC operation. Both experiments and simulations show that modulation of the potential at the ring electrodes, which yields a conversion ratio ≥0.97 over a broad range of conditions, can control the reaction at the disk electrodes. High collection efficiency and small charging current at the collector electrode point the way to obtaining lower detection limits in electroanalytical experiments, and they also allow measurements at high scan rate. In addition, the combination of high electrode density and small insulator thickness

improves device performance. Integration with a nanochannel further enhances collection efficiency, conversion ratio, and measurement selectivity, while demonstrating the compatibility of the device with a confined geometry and its applicability to lab-on-a-chip systems.

EXPERIMENTAL SECTION

Nanoarray Fabrication. A detailed fabrication procedure for the array of nanoscale-recessed ring-disk electrodes is given in the Supporting Information. Briefly, the device is constructed *via* layer-by-layer deposition of Au, silicon nitride/silicon dioxide, polystyrene nanospheres, and Cr followed by multistep reactive ion etching (RIE). A schematic diagram of the macroscopic layout, cross section, and SEM images of the array is given in Figure 1. The arrays fabricated by this NSL approach cover an area of 50 μm $\times$ 50 μm and typically contain $\sim$2000 nanopores (or $\sim$15 pores in the low density array) of $\sim$500 nm diameter and $\sim$1.0 μm spacing. For the nanochannel-confined measurements, a 5 mm long, 25 μm wide, 200 nm high channel was constructed directly on top of the recessed ring-disk array. This was achieved by coating the substrate with 200 nm silicon nitride, patterning by photolithography, and etching with RIE. A piece of PDMS with two wells separated by $\sim$5 mm was aligned with, and sealed to, the nanochannel under an optical microscope. After being sealed with a PDMS top layer, the nanochannels were filled with solution under vacuum.

Electrochemical Characterization. Cyclic voltammetry (CV) experiments were conducted on a CHI bipotentiostat (840c, CH Instruments Inc.) using a platinum wire and a Ag/AgCl electrode as auxiliary and reference electrodes, respectively. In all CV measurements, the potential of the disk electrodes is swept, and the ring electrodes are held at a constant potential (GC mode) or disconnected (non-GC mode).

Simulations. Finite element simulations were performed in COMSOL Multiphysics version 4.3. An array of 10 nanopores was simulated in a 2D geometry, consisting of 10 recessed disk electrodes (r = 250 nm), a 200 nm thick insulating layer, a 200 nm thick ring electrode layer, and a 200 nm high top insulator layer. The domain above the pores was drawn sufficiently large (w = 600 μm, h = 400 μm) to avoid interference from boundaries, and the mesh was refined both within the nanopores and in the region just above the pores to avoid misleading results. Time-dependent simulations were performed using 122,148 geometric elements. Details of the simulations are given in the Supporting Information.

Conflict of Interest: The authors declare no competing financial interest.

Acknowledgment. This work was supported by the National Science Foundation Grant 1111739 (C.M.), NSF Grant 0852741 (L.R.G.), and the Department of Energy Basic Energy Sciences Grant DE FG02 07ER15851 (N.M.C.). Fabrication and structural characterization of the devices studied here were accomplished at the Notre Dame Nanofabrication Facility and the Notre Dame Integrated Imaging Facility whose generous support is gratefully acknowledged.

Supporting Information Available: Fabrication procedure as well the simulations of electrochemical behavior in detail. This material is available free of charge *via* the Internet at http://pubs.acs.org.

REFERENCES AND NOTES

1. Dawson, K.; Wahl, A.; Murphy, R.; O'Riordan, A. Electroanalysis at Single Gold Nanowire Electrodes. *J. Phys. Chem. C* **2012**, *116*, 14665–14673.
2. Menon, V. P.; Martin, C. R. Fabrication and Evaluation of Nanoelectrode Ensembles. *Anal. Chem.* **1995**, *67*, 1920–1928.
3. Nagale, M. P.; Fritsch, I. Individually Addressable, Submicrometer Band Electrode Arrays. 1. Fabrication from Multilayered Materials. *Anal. Chem.* **1998**, *70*, 2902–2907.
4. Dudin, P. V.; Snowden, M. E.; Macpherson, J. V.; Unwin, P. R. Electrochemistry at Nanoscale Electrodes: Individual Single-Walled Carbon Nanotubes (SWNTs) and SWNT-Templated Metal Nanowires. *ACS Nano* **2011**, *5*, 10017–10025.
5. Hees, J.; Hoffmann, R.; Kriele, A.; Smirnov, W.; Obloh, H.; Glorer, K.; Raynor, B.; Driad, R.; Yang, N.; Williams, O. A.; *et al.* Nanocrystalline Diamond Nanoelectrode Arrays and Ensembles. *ACS Nano* **2011**, *5*, 3339–3346.
6. Branagan, S. P.; Contento, N. M.; Bohn, P. W. Enhanced Mass Transport of Electroactive Species to Annular Nanoband Electrodes Embedded in Nanocapillary Array Membranes. *J. Am. Chem. Soc.* **2012**, *134*, 8617–8624.
7. Dawson, K.; Baudequin, M.; O'Riordan, A. Single On-Chip Gold Nanowires for Electrochemical Biosensing of Glucose. *Analyst* **2011**, *136*, 4507–4513.
8. Aguilar, Z. P.; Vandaveer, W. R. I. V.; Fritsch, I. Self-Contained Microelectrochemical Immunoassay for Small Volumes Using Mouse IgG as a Model System. *Anal. Chem.* **2002**, *74*, 3321–3329.
9. Gasparac, R.; Taft, B. J.; Lapierre-Devlin, M. A.; Lazareck, A. D.; Xu, J. M.; Kelley, S. O. Ultrasensitive Electrocatalytic DNA Detection at Two- and Three-Dimensional Nanoelectrodes. *J. Am. Chem. Soc.* **2004**, *126*, 12270–12271.
10. Wolfrum, B.; Zevenbergen, M.; Lemay, S. Nanofluidic Redox Cycling Amplification for the Selective Detection of Catechol. *Anal. Chem.* **2008**, *80*, 972–977.
11. Arrigan, D. W. M. Nanoelectrodes, Nanoelectrode Arrays and Their Applications. *Analyst* **2004**, *129*, 1157–1165.
12. Bard, A. J.; Crayston, J. A.; Kittlesen, G. P.; Varco, S. T.; Wrighton, M. S. Digital Simulation of the Measured Electrochemical Response of Reversible Redox Couples at Microelectrode Arrays: Consequences Arising from Closely Spaced Ultramicroelectrodes. *Anal. Chem.* **1986**, *58*, 2321–2331.
13. Niwa, O.; Morita, M.; Tabei, H. Electrochemical Behavior of Reversible Redox Species at Interdigitated Array Electrodes with Different Geometries: Consideration of Redox Cycling and Collection Efficiency. *Anal. Chem.* **1990**, *62*, 447–452.
14. Ueno, K.; Hayashida, M.; Ye, J.-Y.; Misawa, H. Fabrication and Electrochemical Characterization of Interdigitated Nanoelectrode Arrays. *Electrochem. Commun.* **2005**, *7*, 161–165.
15. Gibson, L. R., II; Branagan, S. P.; Bohn, P. W. Convective Delivery of Electroactive Species to Annular Nanoband Electrodes Embedded in Nanocapillary-Array Membranes. *Small* **2013**, *9*, 90–97.
16. Niwa, O.; Tabei, H. Voltammetric Measurements of Reversible and Quasi-reversible Redox Species Using Carbon Film Based Interdigitated Array Microelectrodes. *Anal. Chem.* **1994**, *66*, 285–289.
17. Hayashi, K.; Takahashi, J.-i.; Horiuchi, T.; Iwasaki, Y.; Haga, T. Development of Nanoscale Interdigitated Array Electrode as Electrochemical Sensor Platform for Highly Sensitive Detection of Biomolecules. *J. Electrochem. Soc.* **2008**, *155*, J240–J243.
18. Odijk, M.; Olthuis, W.; Dam, V. A. T.; van den Berg, A. Simulation of Redox-Cycling Phenomena at Interdigitated Array (IDA) Electrodes: Amplification and Selectivity. *Electroanalysis* **2008**, *20*, 463–468.
19. Goluch, E. D.; Wolfrum, B.; Singh, P. S.; Zevenbergen, M. A. G.; Lemay, S. G. Redox Cycling in Nanofluidic Channels Using Interdigitated Electrodes. *Anal. Bioanal. Chem.* **2009**, *394*, 447–456.
20. Rahimi, M.; Mikkelsen, S. R. Cyclic Biamperometry at Microinterdigitated Electrodes. *Anal. Chem.* **2011**, *83*, 7555–7559.
21. Postlethwaite, T. A.; Hutchison, J. E.; Murray, R.; Fosset, B.; Amatore, C. Interdigitated Array Electrode as an Alternative

to the Rotated Ring-Disk Electrode for Determination of the Reaction Products of Dioxygen Reduction. *Anal. Chem.* **1996**, *68*, 2951–2958.
22. Barnes, E. O.; Lewis, G. E. M.; Dale, S. E. C.; Marken, F.; Compton, R. G. Generator–Collector Double Electrode Systems: A Review. *Analyst* **2012**, *137*, 1068–1081.
23. Bartelt, J. E.; Deakin, M. R.; Amatore, C.; Wightman, R. M. Construction and Use of Paired and Triple Band Microelectrodes in Solutions of Low Ionic Strength. *Anal. Chem.* **1988**, *60*, 2167–2169.
24. Fosset, B.; Amatore, C.; Bartelt, J.; Wightman, R. M. Theory and Experiment for the Collector–Generator Triple-Band Electrode. *Anal. Chem.* **1991**, *63*, 1403–1408.
25. Paixao, T. R. L. C.; Richter, E. M.; Brito-Neto, J. G. A.; Bertotti, M. Fabrication of a New Generator–Collector Electrochemical Microdevice: Characterization and Applications. *Electrochem. Commun.* **2006**, *8*, 9–14.
26. Straver, M. G.; Odijk, M.; Olthuis, W.; van den Berg, A. A Simple Method To Fabricate Electrochemical Sensor Systems with Predictable High-Redox Cycling Amplification. *Lab Chip* **2012**, *12*, 1548–1553.
27. Vandaveer, W. R. I. V.; Woodward, D. J.; Fritsch, I. Redox Cycling Measurements of a Model Compound and Dopamine in Ultrasmall Volumes with a Self-Contained Microcavity Device. *Electrochim. Acta* **2003**, *48*, 3341–3348.
28. Neugebauer, S.; Mueller, U.; Lohmueller, T.; Spatz, J. P.; Stelzle, M.; Schuhmann, W. Characterization of Nanopore Electrode Structures as Basis for Amplified Electrochemical Assays. *Electroanalysis* **2006**, *18*, 1929–1936.
29. Menshykau, D.; del Campo, F. J.; Muñoz, F. X.; Compton, R. G. Current Collection Efficiency of Micro- and Nano-Ring-Recessed Disk Electrodes and of Arrays of These Electrodes. *Sens. Actuators, B* **2009**, *138*, 362–367.
30. Menshykau, D.; Cortina-Puig, M.; del Campo, F. J.; Muñoz, F. X.; Compton, R. G. Plane-Recessed Disk Electrodes and Their Arrays in Transient Generator–Collector Mode: The Measurement of the Rate of the Chemical Reaction of Electrochemically Generated Species. *J. Electroanal. Chem.* **2010**, *648*, 28–35.
31. Zhu, F.; Yan, J.-W.; Lu, M.; Zhou, Y.-L.; Yang, Y.; Mao, B.-W. A Strategy for Selective Detection Based on Interferent Depleting and Redox Cycling Using the Plane-Recessed Microdisk Array Electrodes. *Electrochim. Acta* **2011**, *56*, 8101–8107.
32. Menshykau, D.; O'Mahony, A. M.; del Campo, F. J.; Muñoz, F. X.; Compton, R. G. Microarrays of Ring-Recessed Disk Electrodes in Transient Generator–Collector Mode: Theory and Experiment. *Anal. Chem.* **2009**, *81*, 9372–9382.
33. Feldman, B. J.; Feldberg, S. W.; Murray, R. W. An Electrochemical Time-of-Flight Experiment. *J. Phys. Chem.* **1987**, *91*, 6558–6560.
34. Amatore, C.; Sella, C.; Thouin, L. Electrochemical Time-of-Flight Responses at Double-Band Generator-Collector Devices under Pulsed Conditions. *J. Electroanal. Chem.* **2006**, *593*, 194–202.
35. Hayashi, K.; Iwasaki, Y.; Horiuchi, T.; Sunagawa, K.; Tate, A. Selective Detection of a Catecholamine against Electroactive Interferents Using an Interdigitated Heteroarray Electrode Consisting of a Metal Oxide Electrode and a Metal Band Electrode. *Anal. Chem.* **2005**, *77*, 5236–5242.
36. Sandison, M. E.; Cooper, J. M. Nanofabrication of Electrode Arrays by Electron-Beam and Nanoimprint Lithographies. *Lab Chip* **2006**, *6*, 1020–1025.
37. Li, H.; Wu, N. A Large-Area Nanoscale Gold Hemisphere Pattern as a Nanoelectrode Array. *Nanotechnology* **2008**, *19*, 275301–275306.
38. Nagale, M. P.; Fritsch, I. Individually Addressable, Submicrometer Band Electrode Arrays. 2. Electrochemical Characterization. *Anal. Chem.* **1998**, *70*, 2908–2913.
39. Henry, C. S.; Fritsch, I. Microcavities Containing Individually Addressable Recessed Microdisk and Tubular Nanoband Electrodes. *J. Electrochem. Soc.* **1999**, *146*, 3367–3373.
40. Neugebauer, S.; Evans, S. R.; Aguilar, Z. P.; Mosbach, M.; Fritsch, I.; Schuhmann, W. Analysis in Ultrasmall Volumes: Microdispensing of Picoliter Droplets and Analysis without Protection from Evaporation. *Anal. Chem.* **2004**, *76*, 458–463.
41. Guo, J.; Lindner, E. Cyclic Voltammograms at Coplanar and Shallow Recessed Microdisk Electrode Arrays: Guidelines for Design and Experiment. *Anal. Chem.* **2009**, *81*, 130–138.
42. Bond, A. M.; Luscombe, D.; Oldham, K. B.; Zoski, C. G. A Comparison of the Chronoamperometric Response at Inlaid and Recessed Disk Microelectrodes. *J. Electroanal. Chem. Interfacial Electrochem.* **1988**, *249*, 1–14.
43. Godino, N.; Borrise, X.; Muñoz, F. X.; del Campo, F. J.; Compton, R. G. Mass Transport to Nanoelectrode Arrays and Limitations of the Diffusion Domain Approach: Theory and Experiment. *J. Phys. Chem. C* **2009**, *113*, 11119–11125.
44. Dam, V. A. T.; Olthuis, W.; van den Berg, A. Redox Cycling with Facing Interdigitated Array Electrodes as a Method for Selective Detection of Redox Species. *Analyst* **2007**, *132*, 365–370.
45. Zevenbergen, M. A. G.; Wolfrum, B. L.; Goluch, E. D.; Singh, P. S.; Lemay, S. G. Fast Electron-Transfer Kinetics Probed in Nanofluidic Channels. *J. Am. Chem. Soc.* **2009**, *131*, 11471–11477.
46. Lewis, P. M.; Sheridan, L. B.; Gawley, R. E.; Fritsch, I. Signal Amplification in a Microchannel from Redox Cycling with Varied Electroactive Configurations of an Individually Addressable Microband Electrode Array. *Anal. Chem.* **2010**, *82*, 1659–1668.